Oxygen Vacancy-Driven High-Performance V_2O_5 Cathodes for Aqueous Manganese Metal Batteries

Sangki Lee, Hyungjin Lee, Hyeonjun Lee, Seunghyeop Baek, Netanel Shpigel, Daniel Sharon, Seung-Tae Hong* (iD)*, and Munseok S. Chae** (iD)

Aqueous batteries are an emerging next-generation technology for large-scale energy storage. Among various metal-ion systems, manganese-based batteries have attracted significant interest due to their superior theoretical energy density over zinc-based battery systems. This study demonstrates oxygen vacancy-engineered vanadium oxide ($V_2O_{4.85}$) as a high-performance cathode material for aqueous manganese metal batteries. The $V_2O_{4.85}$ cathode had a discharge capacity of 212.6 mAh g^{-1} at 0.1 A g^{-1}, retaining 89.5% capacity after 500 cycles. Oxygen vacancies enhanced ion diffusion and reduced migration barriers, facilitating both Mn^{2+} and H^+ ion intercalation. Proton intercalation dominated charge storage, forming $Mn(OH)_2$ layers, whereas Mn^{2+} contributed to surface-limited reactions. Furthermore, manganese metal batteries had a significantly higher operating voltage than that of aqueous zinc battery systems. Despite challenges with hydrogen evolution reactions at the Mn metal anode, this study underscores the potential of manganese batteries for future energy storage systems.

1. Introduction

Lithium-ion batteries (LIBs) have been widely adopted as alternatives to fossil fuels in various energy storage systems owing to their high energy density and rechargeability.[1] Despite their benefits, conventional LIBs face challenges such as the scarcity of lithium resources and the use of flammable organic electrolytes. Considering the growing demand for large-scale energy storage, which necessitates the use of a massive number of batteries with high safety regulations, aqueous rechargeable batteries have emerged as a promising alternative to lithium-ion batteries.[2] These batteries use non-flammable, water-based electrolytes, offering superior fire safety and cost-effectiveness compared to traditional LIBs. Additionally, aqueous electrolytes exhibit higher ionic conductivity compared to the organic electrolytes employed in conventional LIBs, thereby facilitating enhanced charge and discharge rates. Battery systems employing aqueous electrolytes are categorized based on the use of monovalent metal ions (Li^+,[3] Na^+,[4,5] K^+[6]) and/or multivalent metal ions (Zn^{2+},[7,8] Ca^{2+},[9,10] Mg^{2+},[11] Al^{3+}[12]).

Although various metal ions are available, Mn^{2+}-based energy storage technologies have recently garnered significant attention as new aqueous battery systems for large-scale energy storage.[13,14] The manganese ion is theoretically capable of transferring more than two electrons per ion, resulting in a higher volumetric energy density. Manganese metal exhibits a low reduction/oxidation potential (-1.19 V vs SHE) and a high theoretical gravimetric capacity (976 mAh g^{-1}), which enables a higher operating voltage for manganese-based battery systems compared to zinc-ion batteries.[15]

Nevertheless, one of the major hindrances to the development of manganese-based batteries is the occurrence of hydrogen evolution reactions (HER) from the electrolyte, which deteriorates efficiency and makes them less favorable for aqueous battery systems.[16] Consequently, research on electrode materials for manganese-based batteries has been scarce, highlighting the need for extensive investigation into new cathode materials. To date, a few manganese battery cathodes have been reported, including Chevrel phase (Mo_6S_8),[17] bilayered-vanadium oxide structures ($Al_{0.1}V_2O_5 \cdot 1.5H_2O$,[18] $Mn_{0.18}V_2O_5 \cdot nH_2O$[19]), V_2O_5,[17] VO_2,[20] $Ag_{0.33}V_2O_5$,[14,21] $Ag_{0.1}V_2O_5$,[22] Prussian blue framework (nickel hexacyanoferrate),[17] and organic electrodes: graphite,[23] PTCDA,[24,25] and coronene.[14] Nevertheless, these electrode materials remain insufficient to achieve the high energy density demanded for advanced applications. Therefore, high-performance electrode materials must be developed for Mn-ion batteries.

The V_2O_5 structure has been extensively considered a cathode material for zinc-ion batteries. One group recently applied V_2O_5 in manganese-ion batteries; however, in this early study, the reported capacity (~73 mAh g^{-1}) was significantly lower than the documented values obtained for typical vanadium-based cathodes for zinc-ion

S. Lee, H. Lee, S. Baek, Prof. M. S. Chae
Department of Nanotechnology Engineering, Pukyong National University, Busan 48547, Korea
E-mail: mschae@pknu.ac.kr
H. Lee, Prof. S.-T. Hong
Department of Energy Science and Engineering, DGIST, Daegu 42988, Korea
E-mail: st.hong@dgist.ac.kr
Prof. N. Shpigel
Department of Chemical Sciences, Ariel University, Ariel 40700, Israel
Prof. D. Sharon
Institute of Chemistry, The Hebrew University of Jerusalem, Jerusalem 9190401, Israel
Prof. S.-T. Hong
Department of Chemistry and Chemical Biology, University of New Mexico, Albuquerque, NM 87131, USA

(iD) The ORCID identification number(s) for the author(s) of this article can be found under https://doi.org/10.1002/eem2.70036.
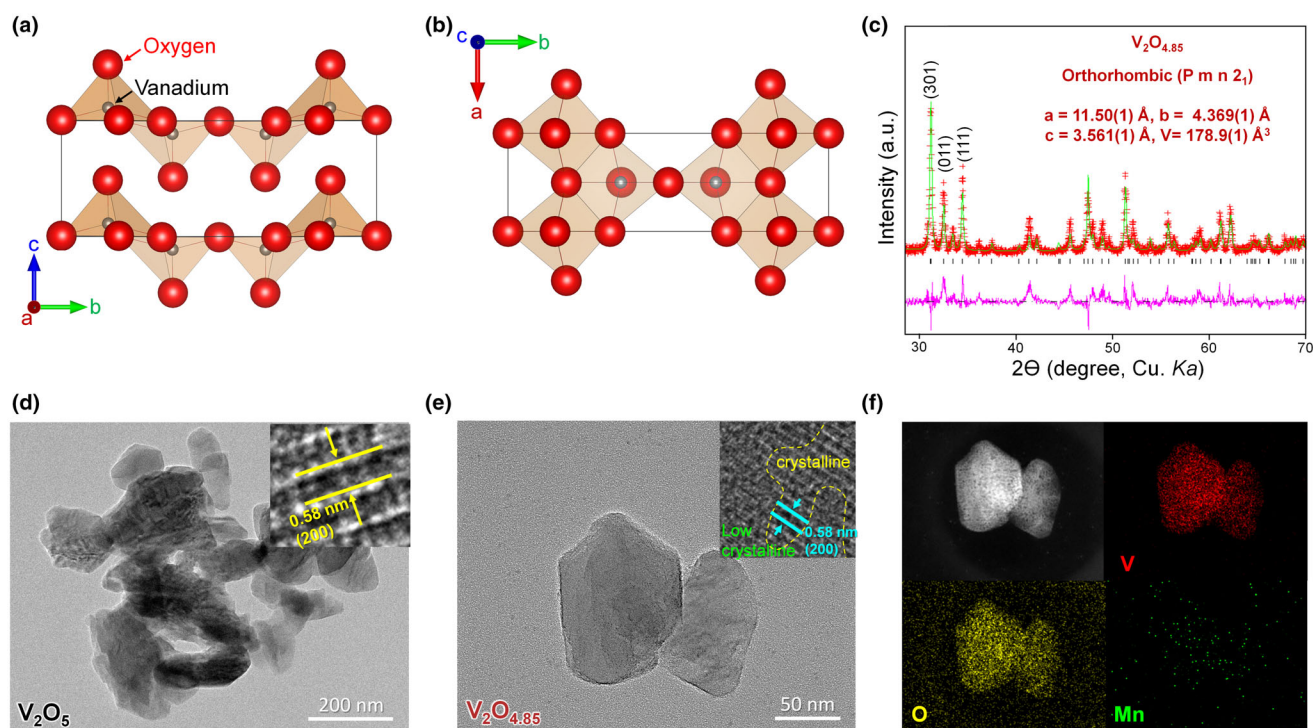
Figure 1. Crystal structure of ideal V_2O_5: a) *bc* plane, b) *ab* plane, c) Rietveld refinement results of as-prepared $V_2O_{4.85}$; TEM images of d) V_2O_5 and e) oxygen-deficient $V_2O_{4.85}$ powder, along with their respective high-resolution lattice fringes; and f) TEM-EDX elemental mapping of V_2O_{5-x} powder.

batteries (ranging between 200 and 350 mAh g^{-1}), indicating the need for further improvement and optimization.[17]

Structural modification and morphology control have been considered to enhance the electrochemical activity of V_2O_5. Controlling the structural defects can significantly influence the electrochemical performance of V_2O_5. For instance, an oxygen vacancy, which is a common defect in transition metal oxides, plays a crucial role in tuning the electronic structure, electrical conductivity, and surface properties of these materials.[26,27] Controlled generation and regulation of oxygen vacancies in transition metal oxide-based cathodes can enhance manganese ion diffusion and improve electronic conductivity. We hypothesize that increasing the oxygen defects can enhance the cation migration by lowering the energy barrier at the V_2O_5 crystal structure in manganese-ion batteries. However, materials with controlled vacancies are difficult to synthesize due to their thermodynamic instability. Therefore, precise control of synthesis conditions is crucial to achieve the desired material.

In this study, vanadium oxide with oxygen vacancies (V_2O_{5-x}) was demonstrated as a high-performance cathode material for aqueous manganese batteries. The V_2O_{5-x} cathode exhibited an impressive discharge capacity of approximately 212.6 mAh g^{-1} at 0.1 A g^{-1} and retained 89.5% of its initial capacity after 500 cycles. Detailed spectroscopic analyses and diffusion pathway calculations revealed the role of H$^+$ and Mn^{2+} ions in the charge storage mechanism of the V_2O_{5-x} structure. The oxygen vacancy-containing structure exhibited a lower migration barrier compared to the crystalline V_2O_5 structure. Finally, a comparative analysis with zinc and manganese metal systems highlighted the potential advantages of manganese metal batteries for future large-scale energy storage applications.

2. Results and Discussion

2.1. Materials Characterization of V_2O_5 and $V_2O_{4.85}$

Figure 1a,b illustrates the crystal structure of V_2O_5, which adopts an orthorhombic system (Pmn2$_1$ space group) composed of VO$_5$ square pyramids with a central V^{5+} ion coordinated by five oxygen atoms. These polyhedral units form layered frameworks (Figure 1a), providing the structural flexibility necessary for ion intercalation. However, highly crystalline V_2O_5 exhibits low electrochemical performance due to the strong oxygen binding forces between the cations. To enhance the electrochemical activity of V_2O_5, we controlled the structural defects, as these can significantly improve electronic conductivity and ion transport—both critical for optimal cathode performance. In general, vacancy formation in oxide materials is influenced by factors, such as temperature, baking time, and the quenching process. Here, we synthesized both pristine V_2O_5 and vacancy-containing V_2O_{5-x} structures using the sol–gel method under controlled thermal heating times to explore these effects. By regulating the oxidation process from vanadium oxalate (gel) to the V_2O_5 structure, we found that limiting the oxidation time prevented full oxidation, thereby inducing the formation of oxygen vacancies.

In brief, bulk V_2O_5 and oxalic acid were dissolved in deionized water and dried at 80 °C. The dried sol was then hand-ground and heated at 400 °C for 1 and 4 h, respectively.[26,28,29] The detailed processes are described in Supporting Information.

Rietveld refinement was performed using GSAS[30] on the powder X-ray diffraction (XRD) data to validate the as-prepared V_2O_{5-x}, as illustrated in Figure 1c. An orthorhombic phase within the same space

group ($Pmn2_1$) was confirmed with the following lattice parameters: $a = 11.50(1)$ Å, $b = 4.369(1)$ Å, and $c = 3.561(1)$ Å. Oxygen vacancies were identified at the 4b sites within the V_2O_5 framework, with an estimated concentration of 0.15 M. Detailed structural parameters are provided in Tables S1 and S2, and Figure S1, Supporting Information. Figure 1d presents transmission electron microscopy (TEM) images of V_2O_5, revealing particle sizes in the 150 nm range. The highly crystalline lattice fringes exhibit a spacing of 0.58 nm, corresponding to the (200) plane of orthorhombic V_2O_5 (Figure 1d, inset). In contrast, Figure 1e illustrates that the oxygen-deficient $V_2O_{4.85}$ has smaller particle sizes, approximately 100 nm. This structure promotes the coexistence of both crystalline and amorphous regions within the V_2O_5 framework (Figure 1e, inset). The d-spacing of V_2O_5 is measured as 3.564 Å. In comparison, the vacancy-containing $V_2O_{4.85}$ exhibits a slight shrinkage of 0.1%, reducing the d-spacing to 3.561 Å. This contraction is likely due to the presence of oxygen vacancies, which induce structural stabilization by reducing the interlayer spacing.

The SEM images are provided in Figures S2 and S3, Supporting Information. TEM-EDX elemental mapping images (Figure 1f) clearly reveal the presence of vanadium and oxygen in the $V_2O_{4.85}$ sample.

2.2. Electrochemical Charge Storage Performances of V_2O_5 and $V_2O_{4.85}$

To systematically investigate the role of oxygen vacancies in modulating the electrochemical performance of aqueous manganese-ion batteries, the pristine V_2O_5 electrodes were compared with oxygen vacancy-engineered $V_2O_{4.85}$ electrodes. Three-electrode cells were used for cathode characterization. Severe HER occurred when Mn metal was used as the anode, hindering the accurate evaluation of the cathode performance. To avoid the HER side reaction, activated carbon was used as the counter electrode, and an Ag/AgCl reference electrode was employed. This three-electrode cell ensured that the working electrode (our cathode material) was tested under controlled conditions, minimizing interference from other side reactions. The saturated $MnCl_2$ aqueous solution (pH: 3.8) was utilized as an electrolyte solution. The cyclic voltammetry (CV) curves in **Figure 2a** were obtained over a voltage range of −0.8 to 0.7 V (vs Ag/AgCl) with a scan rate of 0.2 mV s^{-1}. Compared to the pristine electrode, the CV profiles revealed an increase in the overall current in the integrated area under the oxidation and reduction regions for the $V_2O_{4.85}$ electrode corresponding to the increased capacity of this structure. This enhancement suggests that oxygen vacancies augment the redox activity by providing additional electrochemically active sites. Such modification facilitates more efficient electron and ion transfer pathways, thereby leading to an overall improvement in specific capacity. Additionally, the sharp and distinct redox peaks observed in the CV curves indicate the reversible manganization and demanganization of the vanadium oxide structures, further confirming the electrochemical robustness of both electrodes. A detailed analysis of galvanostatic discharge–charge (GDC) profiles under a current density of 0.1 A g^{-1} reveals that the $V_2O_{4.85}$ electrode delivers a substantially higher discharge capacity (212.6 mAh g^{-1}) compared to the pristine V_2O_5 electrode (172.0 mAh g^{-1}), as illustrated in Figure 2b. Furthermore, rate performance evaluations conducted across a range of current densities (0.1, 0.2, 0.4, and 0.8 A g^{-1}) highlight the higher capacity retention of the $V_2O_{4.85}$ electrode under high-rate conditions (Figure 2c). The discharge capacities of $V_2O_{4.85}$ were 191.9, 177.2, and 160.0 mAh g^{-1} at current densities

of 0.2, 0.4, and 0.8 A g^{-1}, respectively. In comparison, the discharge capacities of V_2O_5 were 157.6, 143.8, and 129.8 mAh g^{-1} at the same current densities. These results demonstrate the critical role of oxygen vacancies in promoting high-rate capability and improved charge storage dynamics. Long-term cycling stability tests at a current density of 0.8 A g^{-1} for 500 cycles underscore the substantial differences in the durability of both electrodes. The capacity of the pristine V_2O_5 electrode drastically degraded, retaining only 65.4% of its initial specific capacity (129.8 mAh g^{-1}) after 500 cycles, accompanied by unstable Coulombic efficiency (CE). The instability of the CE may arise from the high migration barrier of crystalline V_2O_5. This high migration barrier leads to significant polarization during the charge–discharge process, resulting in a reduced charge capacity. In contrast, the $V_2O_{4.85}$ electrode retained a specific capacity of 170.2 mAh g^{-1} with an exceptional capacity retention of approximately 89.5%, coupled with a stable CE, as depicted in Figure 2d.

The unit cell volume of V_2O_5 is 179.4 Å^3, whereas that of $V_2O_{4.85}$ is reduced to 178.9 Å^3, indicating a 0.28% contraction (Figure 1c and Figure S1, Supporting Information). In most cases, a reduction in unit cell volume can shorten ion diffusion pathways within the crystal structure, leading to negative effects on electrochemical performance. However, in $V_2O_{4.85}$, the presence of oxygen vacancies compensates for this effect, resulting in enhanced electrochemical performance.

To further elucidate the reaction kinetics and underlying electrochemical mechanisms, CV measurements were conducted at varying scan rates, as illustrated in Figure 2f. The observed shifts in oxidation and reduction peak positions with increasing scan rates are indicative of fast ion and electron transport kinetics in the $V_2O_{4.85}$ electrode. A power-law analysis was conducted to differentiate surface-limited capacitive behavior from diffusion-controlled kinetics. The calculated power-law coefficients (b-values) for the primary redox peaks are 0.542 and 0.759 at the 0.0 V range versus Ag/AgCl (Figure 2g), indicating a significant contribution from surface-limited capacitive processes. Further analysis revealed that approximately 76.8% of the manganese and/or proton ions were involved in diffusion-controlled reactions with $V_2O_{4.85}$ (Figure 2h and Figure S4, Supporting Information). However, V_2O_5 exhibits a much lower intercalation-based reaction; specifically, the intercalation contributions for V_2O_5 are 33.3%. This indicates that our vacancy-containing structure facilitates easier cation intercalation (Figure S5, Supporting Information). These findings highlight the interplay between surface-dominated capacitive reactions and minor bulk diffusion mechanisms in charge storage for low-crystalline $V_2O_{4.85}$, emphasizing the critical role of surface redox reactions in achieving its high-rate charge–discharge performance. To understand Mn and proton insertion, we conducted Inductively Coupled Plasma (ICP) analysis (Table S3, Supporting Information). The results indicate that 0.48 M of Mn reacts with V_2O_5, contributing approximately 142 mAh g^{-1} to the total capacity, while the remaining 70.6 mAh g^{-1} is likely attributed to H$^+$ intercalation.

2.3. Charge Storage Mechanism of $V_2O_{4.85}$

TEM-EDX elemental mapping and X-ray photoelectron spectroscopy (XPS) analyses were performed (**Figure 3**) to explore the charge storage mechanism of the electrode. The discharge process was evaluated at five key states: the pristine state (OCV ~0.7 V), during discharge to 0.1, −0.1, and −0.35 V, and the fully discharged state at −0.9 V, referenced against Ag/AgCl, as depicted in Figure 3a. In the pristine
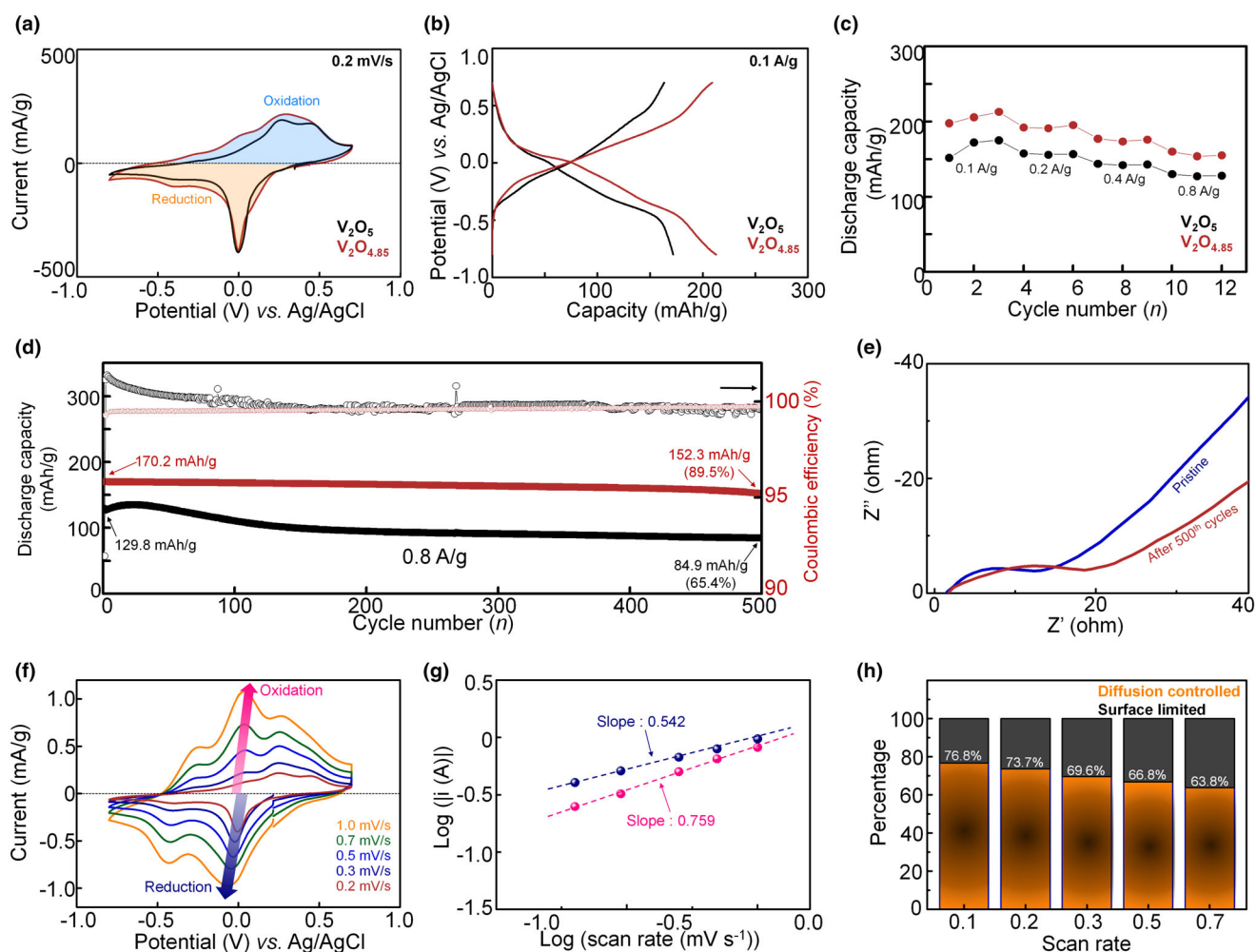
Figure 2. Electrochemical performance of vanadium oxides with/without oxygen vacancies: a) cyclic voltammogram at 0.2 mV s^{-1}, b) galvanostatic discharge–charge (GDC) profile at 0.1 A g^{-1}, c) rate performance under varying current densities, and d) cycling performance and capacity retention at 0.8 A g^{-1}. e) Nyquist plots of the pristine electrode and that after the 500th cycle. f) CV curves of $V_2O_{4.85}$ obtained at varying scan rates from 0.2 to 1.0 mV s^{-1}. g) Analysis of b values derived from the correlation between cathodic peak current and scan rate. h) Evaluation of the contributions of surface-limited and diffusion-controlled ion reactions in $V_2O_{4.85}$.

state, Mn signals were not detected; however, in the fully discharged state (-0.9 V vs Ag/AgCl), Mn was clearly observed across the electrode alongside vanadium and oxygen. This indicates that Mn ions participated in the charge storage process with material during discharge, as illustrated in Figure 3b,c. In the charged state, the Mn signal weakens but remains detectable, as presented in Figure S6, Supporting Information, suggesting that Mn contributes to charge storage through capacitance or intercalation reactions. TEM-EDX spectra for the pristine, discharged, and charged samples are provided in Figures S7–S9, Supporting Information.

Figure 3d–f illustrates the XPS spectra for vanadium, oxygen, and manganese. As the electrode transitions from the initial to the fully discharged state, the V^{5+} ($2p_{3/2}$) peak at 517.2 eV shifts slightly to 516.5 eV, corresponding to V^{4+} ($2p_{3/2}$), indicating that vanadium participates as a redox center. Interestingly, the intensity of the V^{5+} ($2p_{3/2}$, $2p_{1/2}$) peaks decreased during the discharge process (Figure 3d), which can be attributed to the interaction of Mn ions with the surface

of the $V_2O_{4.85}$ cathode. Conversely, the intensity of the Mn ($2p_{3/2}$, $2p_{1/2}$) peaks increased during the reduction process (Figure 3e), supporting the hypothesis that Mn-containing layers form on the cathode surface. To further investigate manganese side products, the O (1s) peaks were analyzed. The peak at 530.1 eV corresponds to the metal-oxygen bond (V–O in this case), whereas the peak at 532.2 eV is attributed to the O–H bond (Figure 3f). During the discharge process, the intensity of the V–O peak decreased, confirming our hypothesis, whereas the O–H peak intensity increased, indicating the formation of a $Mn(OH)_2$ phase on the surface of the vanadium oxide after discharge.[21]

The formation of $Mn(OH)_2$ is closely related to the observed electrochemical performance. As illustrated in the impedance spectra in Figure 2e, the charge transfer resistance increased significantly after the 500th cycle. This increase is attributed to the formation of $Mn(OH)_2$ on the cathode surface, which contributes to the elevated charge transfer resistance. Unlike the common solid electrolyte interface layer in
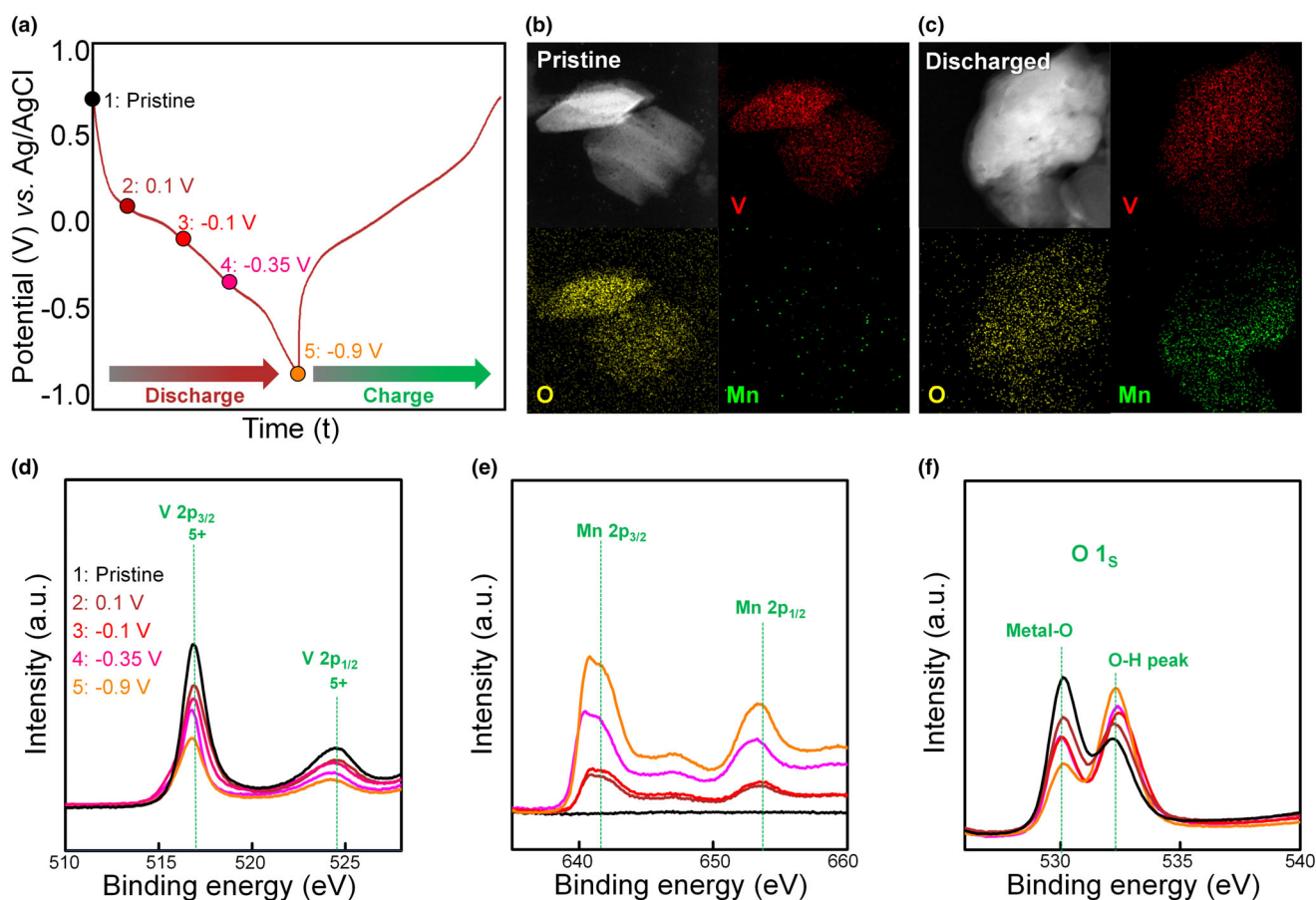
Figure 3. a) Galvanostatic profile of $V_2O_{4.85}$ from pristine to fully discharged (-0.9 V vs Ag/AgCl), TEM-EDX elemental mapping of V, O, and Mn for b) pristine and c) fully discharged states, XPS spectra of d) V 2p, e) Mn 2p, and f) O 1s at pristine, 0.1, -0.1, -0.35, and -0.9 V (fully discharged).

lithium batteries, this $Mn(OH)_2$ layer acts as an insulating layer. To achieve better electrochemical performance, the formation of $Mn(OH)_2$ should be suppressed, potentially through the use of electrolyte additives or by controlling the pH of the electrolyte.

XRD patterns recorded during the discharge process (**Figure 4**a) revealed no manganese hydrate peaks at the early stages of discharge. However, as the discharge progressed to full capacity, these peaks gradually emerged, indicating that Mn^{2+} ions were unable to effectively intercalate into the electrode structure. Instead, they participated in side reactions with the aqueous electrolyte, forming manganese-based compound layers on the electrode surface. Furthermore, during the discharge process, the layered vanadium oxide structure underwent amorphization, as evidenced by the broadening of diffraction peaks. Figure 4b illustrates the mechanism underlying these side reactions.

The migration pathways and barrier of Mn^{2+} and protons (H^+) were analyzed for pristine V_2O_5 and oxygen vacancy-introduced $V_2O_{4.85}$ structures using SoftBV program,[31,32] as illustrated in Figure 4c–j. In the b–c plane of V_2O_5, disconnected regions were identified within the structure, indicating that Mn^{2+} ion migration is hindered due to high migration energy barriers (Figure 4c). In the a–b plane of V_2O_5, Mn^{2+} ions exhibit migration pathways along the a-axis; however, the activation energy for migration is high at 2.806 eV, significantly limiting Mn^{2+} diffusion within the structure (Figure 4d). In contrast, the

introduction of oxygen vacancies into the V_2O_5 structure alters the migration scenario. In the b–c plane of $V_2O_{4.85}$, the disconnected regions are eliminated, enabling Mn^{2+} migration along the c-axis. However, the activation energy remains high at 1.694 eV, restricting diffusion within the structure (Figure 4e). In the a–b plane of $V_2O_{4.85}$, migration pathways were observed along both the a- and b-axis. While oxygen vacancies reduce the activation energy, improving Mn^{2+} migration, the values remain high at 1.361 and 1.894 eV for these directions (Figure 4f).

In aqueous battery systems, protons (H^+) are more favorable for intercalation into the structure compared to Mn^{2+} ions. Proton migration pathways in the V_2O_5 structure span the a-, b-, and c-axes, with lower activation energies of 0.144, 0.164, and 0.722 eV, respectively (Figure 4g,h). In the $V_2O_{4.85}$ structure, disconnected regions persist along the c-axis in the b–c plane, hindering proton migration. However, in the a–b plane, the activation energies are drastically reduced to 0.166 and 0.067 eV, enabling more efficient diffusion into the structure (Figure 4i,j).

In summary, the reaction mechanism of vanadium oxides reveals that introducing oxygen vacancies enhances electrochemical activity. In aqueous manganese systems, both protons and manganese ions can intercalate into the structure. Proton intercalation or HER reaction drives the formation of $Mn(OH)_2$ and hydrate phases, playing a major role in
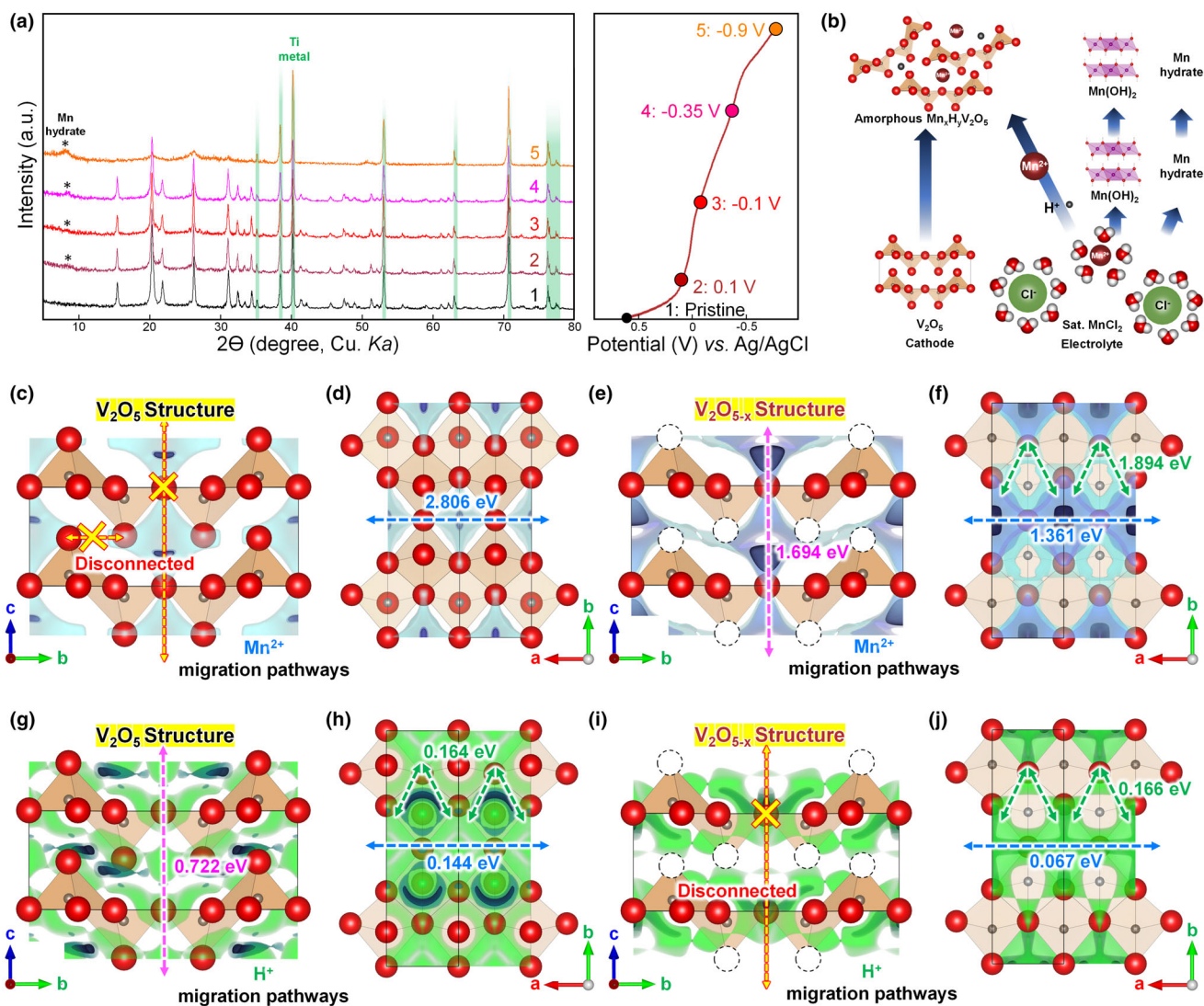
Figure 4. a) Ex situ XRD patterns recorded during the discharge process alongside corresponding electrochemical evaluations. b) Reaction mechanisms between vanadium oxide and the aqueous $MnCl_2$ electrolyte. c, d) Migration pathways and energy barriers for Mn^{2+} ions along the b–c and a–b planes of the crystalline V_2O_5 structure. e, f) Migration pathways and energy barriers for Mn^{2+} ions in the $V_2O_{4.85}$ structure. g, h) Migration pathways and energy barriers for H^+ ions along the b–c and a–b planes of the crystalline V_2O_5 structure. i, j) Migration pathways and energy barriers for H^+ ions in the $V_2O_{4.85}$ structure.

the overall charge storage mechanism. Conversely, manganese-ion intercalation contributes to surface-limited capacitive reactions, with a minor impact on the overall electrochemical performance.

2.4. Comparison of Manganese and Zinc Metal Cell

To evaluate the potential of manganese battery systems to achieve higher operating voltages compared to zinc batteries, electrochemical tests were conducted using Mn and Zn metal anodes in their respective Mn- and Zn-based systems using $MnCl_2$ and $ZnCl_2$ aqueous electrolytes, respectively. **Figure 5a** highlights the theoretical operating voltage difference between Zn and Mn metal battery systems. The redox potential of Mn metal is -1.19 V versus the SHE, which is lower than that

of Zn metal (-0.76 V), suggesting that manganese-based battery systems can achieve higher operating voltages than zinc-based systems. This is further supported by the GDC curve illustrated in Figure 5b, where $V_2O_{4.85}$ cathodes paired with Mn metal in Mn-saturated $MnCl_2$ solutions exhibit higher operating voltages (1.3 V) compared to Zn metal cells (1.0 V) in Zn-saturated $ZnCl_2$ solutions at a current density of 0.1 A g^{-1}. These results show that the Mn metal battery system is a promising postzinc aqueous battery technology.

Figure 5c presents GDC curves measured under varying current densities (0.1, 0.2, 0.4, and 0.8 A g^{-1}). The discharge capacity at 0.1 A g^{-1} is 200.7 mAh g^{-1}, but it drops sharply to 124.8, 120.7, and 97.1 mAh g^{-1} at 0.2, 0.4, and 0.8 A g^{-1}, respectively (Figure 5c, d). The rate performance indicates a significant decrease in discharge capacity with increasing current density compared to experiments using
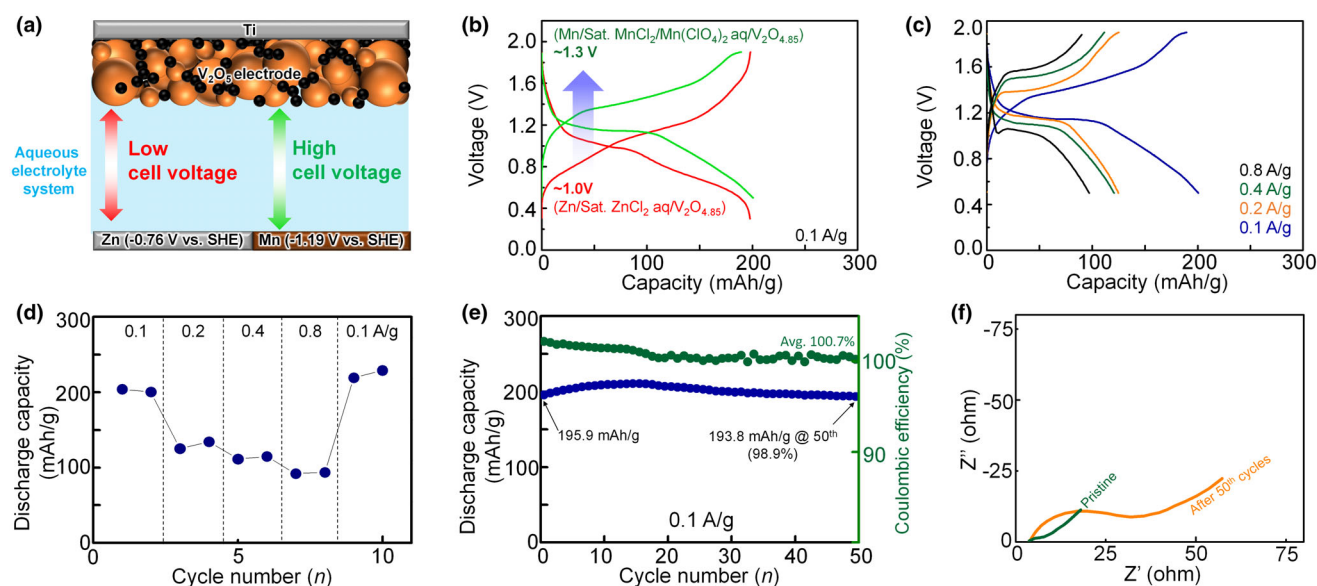
Figure 5. a) Schematic representation of the theoretical operating voltage difference between Zn and Mn metal batteries in aqueous electrolyte systems. b) GDC profile of $V_2O_{4.85}$ using Mn- and Zn-saturated aqueous electrolytes with respective metal anodes at 0.1 A g^{-1}. c) GDC curves and d) rate capability of the Mn-saturated $MnCl_2$ aqueous/$V_2O_{4.85}$ cell at varying current densities. e) Cycling performance of the Mn metal cell at a current density of 0.1 A g^{-1}. f) Nyquist plots of the cell in its pristine state and after 50 cycles.

an activated carbon counter electrode (Figure 2). This lower performance is likely due to the direct use of Mn metal as the anode. During operation in aqueous electrolytes, the HER reaction, a dominant reaction in water electrolysis, generates hydrogen gas, which forms an Mn oxide layer on the Mn metal surface. This oxide layer increases electrical resistance, thereby compromising battery performance.

Meanwhile, Figure 5e demonstrates stable cycling performance and capacity retention at a current density of 0.1 A g^{-1}. The system maintains an initial discharge capacity of 195.9 mAh g^{-1}, with only a slight decrease to 193.8 mAh g^{-1} after 50 cycles, corresponding to a high capacity retention of 98.9%. Although the CE is initially higher than 100%, it stabilizes after 20 cycles. An increase in resistance is observed after cycling, as illustrated in Figure 5f.

However, the direct use of manganese metal as an anode is challenging due to its high chemical reactivity with water, which triggers the HER. This system still has possibilities that Mn is continually consumed upon discharging, while upon charging (Mn extraction from the cathode) you probably have water splitting which compensates the charge from the cathode. This reactivity leads to rapid capacity degradation and performance deterioration of the battery. To address these issues, further research on electrolyte additives and dual-salt electrolyte systems is essential. Despite these challenges, our findings demonstrate that aqueous manganese battery systems can achieve higher operating voltages compared to zinc-ion batteries, highlighting their potential as a promising candidate for future large-scale energy storage applications.

3. Conclusion

This study demonstrates the superior electrochemical performance of oxygen vacancy-engineered $V_2O_{4.85}$ as a high-performance cathode material for aqueous manganese-ion batteries. The $V_2O_{4.85}$ cathode exhibited a remarkable discharge capacity and retained 89.5% of its initial capacity after 500 cycles, outperforming its pristine V_2O_5 counterpart. Spectroscopic analyses and detailed pathway calculations showed that both Mn^{2+} and H^+ ions contribute to the charge storage mechanism. The oxygen vacancies reduced the migration energy barrier for these ions, enhancing the overall electrochemical activity of the cathode material. The vacancies also significantly improved the ion diffusion and charge storage dynamics of the cathode material. Our findings highlight the potential of aqueous manganese batteries for large-scale energy storage applications owing to their higher operating voltages and higher energy densities. Future studies should focus on optimizing electrolyte formulations and electrode materials to enhance the performance and durability of manganese batteries, paving the way for their practical deployment in energy storage systems.

4. Experimental Section

Detailed information related to the synthesis of active electrodes, physicochemical characterization, and electrochemical evaluation of bifunctional electrodes towards UOR and supercapacitor application is provided in Supporting Information.

Acknowledgements

Conflict of Interest

The authors declare no conflict of interest.

Supporting Information

Supporting Information is available from the Wiley Online Library or from the author.

Keywords

[1] M. Armand, J.-M. Tarascon, *Nature* **2008**, *451*, 652.

[2] Y. Liang, Y. Yao, *Nat. Rev. Mater.* **2023**, *8*, 109.

[3] Y. Wang, J. Yi, Y. Xia, *Adv. Energy Mater.* **2012**, *2*, 830.

[4] D. Bin, F. Wang, A. G. Tamirat, L. Suo, Y. Wang, C. Wang, Y. Xia, *Adv. Energy Mater.* **2018**, *8*, 1703008.

[5] M. S. Chae, H. J. Kim, J. Lyoo, R. Attias, Y. Elias, Y. Gofer, S.-T. Hong, D. Aurbach, *ACS Appl. Energy Mater.* **2020**, *3*, 10744.

[6] X. Zhang, T. Xiong, B. He, S. Feng, X. Wang, L. Wei, L. Mai, *Energ. Environ. Sci.* **2022**, *15*, 3750.

[7] G. Fang, J. Zhou, A. Pan, S. Liang, *ACS Energy Lett.* **2018**, *3*, 2480.

[8] C. Xu, B. Li, H. Du, F. Kang, *Angew. Chem. Int. Ed.* **2012**, *51*, 933.

[9] S. Gheytani, Y. Liang, F. Wu, Y. Jing, H. Dong, K. K. Rao, X. Chi, F. Fang, Y. Yao, *Adv. Sci.* **2017**, *4*, 1700465.

[10] M. S. Chae, J. W. Heo, J. Hyoung, S. T. Hong, *ChemNanoMat* **2020**, *6*, 1049.

[11] X. Ye, X. Xiao, Z. Wu, Y. Zhan, X. Wu, S. Liu, *J. Mater. Chem. A* **2024**, *12*, 23337.

[12] X. Wang, Z. Xi, Q. Zhao, *Ind. Chem. Mater.* **2025**, *3*, 7.

[13] M. Wang, Y. Meng, Y. Xu, N. Chen, M. Chuai, Y. Yuan, J. Sun, Z. Liu, X. Zheng, Z. Zhang, *Energ. Environ. Sci.* **2023**, *16*, 5284.

[14] H. Lee, A. Nimkar, H. Lee, N. Shpigel, D. Sharon, S. T. Hong, M. S. Chae, *Energy Environ. Mater.* **2025**, *8*, e12823.

[15] D. Shen, X. Zheng, R. Luo, T. Jiang, M. Wang, M. Zhang, Q. Peng, L. Song, S. Zhou, Z. Hou, *Joule* **2024**, *8*, 780.

[16] M. Wang, Y. Meng, Y. Xu, D. Shen, P. Tong, W. Chen, *ACS Energy Lett.* **2024**, *9*, 1381.

[17] A. Nimkar, M. S. Chae, S. Wee, G. Bergman, B. Gavriel, M. Turgeman, F. Malchik, M. D. Levi, D. Sharon, M. R. Lukatskaya, *ACS Energy Lett.* **2022**, *7*, 4161.

[18] S. Bi, Y. Zhang, S. Deng, Z. Tie, Z. Niu, *Angew. Chem. Int. Ed.* **2022**, *61*, e202200809.

[19] S. Bi, S. Wang, F. Yue, Z. Tie, Z. Niu, *Nat. Commun.* **2021**, *12*, 6991.

[20] M. Li, C. Li, C. Zuo, J. Hu, C. Li, W. Luo, S. Luo, A. Duan, J. Wang, X. Wang, *Adv. Mater.* **2024**, *36*, 2407233.

[21] H. Lee, H. Lee, J. Pyun, S. T. Hong, M. S. Chae, *Adv. Sci.* **2024**, *11*, 2406642.

[22] Z. Fan, Z. Hou, W. Lu, H. Zheng, N. Chen, M. Yao, C. Wang, H. Jiang, D. Zhang, F. Du, *Small* **2025**, *21*, 2406501.

[23] Z. Cheng, Q. Dong, G. Pu, J. Song, W. Zhong, J. Wang, *Small* **2024**, *20*, 2400389.

[24] H. Lee, A. Nimkar, N. Shpigel, D. Sharon, S.-T. Hong, D. Aurbach, M. S. Chae, *ACS Energy Lett.* **2024**, *9*, 5627.

[25] S. Dong, Z. Xu, Z. Cao, H. Ren, J. Yang, J. Zhang, X. Qu, J. Li, X. Dong, *Chem. Eng. J.* **2024**, *501*, 157774.

[26] J. J. Ye, P. H. Li, H. R. Zhang, Z. Y. Song, T. Fan, W. Zhang, J. Tian, T. Huang, Y. Qian, Z. Hou, *Adv. Funct. Mater.* **2023**, *33*, 2305659.

[27] M. S. Chae, A. Chakraborty, S. Kunnikuruvan, R. Attias, S. Maddukuri, Y. Gofer, D. T. Major, D. Aurbach, *Adv. Energy Mater.* **2020**, *10*, 2002077.

[28] S.-C. Lim, J. Lee, H. H. Kwak, J. W. Heo, M. S. Chae, D. Ahn, Y. H. Jang, H. Lee, S.-T. Hong, *Inorg. Chem.* **2017**, *56*, 7668.

[29] D. Zhao, Q. Zhu, X. Li, M. Dun, Y. Wang, X. Huang, *Batteries Supercaps* **2022**, *5*, e202100341.

[30] B. H. Toby, *J. Appl. Cryst.* **2001**, *34*, 210.

[31] H. Chen, L. L. Wong, S. Adams, *Acta Crystallogr. Sect. B: Struct. Sci., Cryst. Eng. Mater.* **2019**, *75*, 18.

[32] L. L. Wong, K. C. Phuah, R. Dai, H. Chen, W. S. Chew, S. Adams, *Chem. Mater.* **2021**, *33*, 625.